Orchard Storage Company LLC

Underground Injection Control – Class VI Permit Application for

Orchard No. 1 to No. 7

Section 2 – Plume Model

Gaines County, Texas

Prepared for *Orchard Storage Company LLC*
Odessa, Texas

By
Lonquist Sequestration, LLC
Austin, TX

May 2023

LONQUIST SEQUESTRATION LLC

SECTION 2 – PLUME MODEL

TABLE OF CONTENTS

Figures

Tables

2.1 Introduction

This section discusses key details of the plume model. The model characterizes the performance of CO_2 injection wells, the 3D spatial distribution of the CO_2 plume, and the associated pressure front over time. It incorporates hydrogeologic data with subsurface flow physics to model the significant physical processes that affect the plume and pressure front evolution. The distribution of the plume and pressure front defines the area of review (AOR) for the well, a corrective action plan if necessary, and the overall viability of the project.

The proposed Orchard No. 1 through No. 7 injection wells were modeled simultaneously to consider the relationship between the wells during injection operations—and to ensure that the plumes of the respective wells do not significantly impact each other within the storage reservoir. This also helps to verify that the pressure of the reservoir remains below the fracture pressure gradient limits of the formation during combined injection operations.

The modeling software used to evaluate this project was Computer Modelling Group's GEM 2022.30 (GEM) simulator. Computer Modelling Group (CMG) has put together one of the most accurate and technically sound reservoir simulation software packages for conventional, unconventional, and secondary recovery. GEM uses equation-of-state (EOS) algorithms and some of the most advanced computational methods to evaluate compositional, chemical, and geochemical processes and characteristics, to produce highly accurate and reliable simulation models for carbon sequestration.

For purposes of injection into a reservoir, CO_2 can be a relatively complex component in the supercritical phase as seen in downhole conditions. The GEM simulator utilizes the compositional methods described, along with equations specific to CO_2, to effectively model and simulate plume behavior within the injection intervals.

The Orchard No. Project will target [redacted] for injection of CO_2. [redacted] the confining interval overlying the injection interval. The dynamic flow model incorporates [redacted] below the impermeable upper confining zone. For purposes of model construction and discussion of the simulation results, the term [redacted]

2.2 Model Inputs

2.2.1 Trapping Mechanisms

The CO_2 injected into the reservoir will take the form of a mobile, CO_2-rich supercritical phase. In this phase, the CO_2 will displace reservoir fluids as it moves laterally and vertically into the reservoir. Viscous forces created by pressure gradients between the higher-pressure wellbore and surrounding reservoir will dominate the initial movement of this CO_2 phase. The most significant flow direction will be radially outward from the higher-pressure wellbore into the surrounding

lower-pressure reservoir. Vertical movement of CO_2 and displaced fluids may occur within the reservoir due to the heterogeneity between layers in the reservoir.

Figure 2-1 illustrates the lateral movement of CO_2 away from Orchard No. 1 at three-year intervals over the 12-year injection period. These panels show that the dominant direction of movement is horizontally away from the wellbore.

After injection ceases, induced pressure gradients away from the wellbore will dissipate. The movement of CO_2 within the reservoir becomes dominantly vertical, driven by gravity and the density contrast between the CO_2 and formation brine (i.e., buoyancy effects). Figure 2-2 shows snapshots of the CO_2 plume over the 50-year interval post-injection. The first panel (image a) illustrates that, at a depth just below [redacted] (see depth scale at left), the layers with the largest plume extent at the end of injection are found. With subsequent time intervals (images b through d), the plume extent in those layers does not expand, but instead moves vertically.

Figures 2-3 through 2-14 then illustrate the same for Orchard No. 2 through No. 7, respectively.

Figure 2-1 – Orchard No. 1 east-west cross-sectional view depicting movement of CO_2 phase during injection.

Figure 2-2 – Orchard No. 1 east-west cross-sectional view depicting movement of CO_2 phase post-injection.

Figure 2-3 – Orchard No. 2 east-west cross-sectional view depicting movement of CO_2 phase during injection.

Figure 2-4 – Orchard No. 2 east-west cross-sectional view depicting movement of CO_2 phase post-injection.

Figure 2-5 – Orchard No. 3 east-west cross-sectional view depicting movement of CO_2 phase during injection.

Figure 2-6 – Orchard No. 3 east-west cross-sectional view depicting movement of CO_2 phase post-injection.

Figure 2-7 – Orchard No. 4 east-west cross-sectional view depicting movement of CO_2 phase during injection.

Figure 2-8 – Orchard No. 4 east-west cross-sectional view depicting movement of CO_2 phase post-injection.

Figure 2-9 – Orchard No. 5 east-west cross-sectional view depicting movement of CO_2 phase during injection.

Figure 2-10 – Orchard No. 5 east-west cross-sectional view depicting movement of CO_2 phase post-injection.

Figure 2-11 – Orchard No. 6 east-west cross-sectional view depicting movement of CO_2 phase during injection.

Figure 2-12 – Orchard No. 6 east-west cross-sectional view depicting movement of CO_2 phase post-injection

Figure 2-13 – Orchard No. 7 east-west cross-sectional view depicting movement of CO_2 phase during injection

Figure 2-14 – Orchard No. 7 east-west cross-sectional view depicting movement of CO_2 phase post-injection

Movement of the CO_2 phase does not continue indefinitely. As the CO_2 moves both vertically and horizontally, various trapping mechanisms immobilize the CO_2 within the reservoir. The most significant trapping mechanism is the presence of the upper confining zone, which stops vertical movement of the CO_2. The other important mechanisms for trapping are residual gas (relative permeability) trapping, dissolution of the CO_2 into formation brines, and condensing of CO_2 into immobile residual oil. Furthermore, trapping can occur from geochemical and structural effects.

2.2.1.1 Upper Confining Zone

Vertical movement of CO_2 will be contained by the low permeability [redacted] will act as a barrier to vertical movement of the relatively buoyant CO_2 through capillary pressure and relative permeability effects.

2.2.1.2 Residual Gas Trapping

While the CO_2 will remain in the supercritical phase within the storage interval ("reservoir"), the gas-liquid relative-permeability relationships will govern fluid flow between the CO_2 and liquid phases present. "CO_2 phase," "supercritical," and "gas" may therefore be used interchangeably in this discussion.

Relative permeability effects on fluid flow depend on the direction of saturation changes. The displacement of brine by injected CO_2 (the *drainage* process) behaves differently than the reverse (the *imbibition* process). During the CO_2 injection, the drainage process controls the relative permeability behavior, as injected CO_2 displaces the brine found in the reservoir. In this process, the non-wetting phase occupies the most favorable flow channels, allowing the CO_2 to be mobile at very low initial saturations. When water is displacing CO_2 under the imbibition process, the increasing saturations of the brine will bypass volumes of CO_2, leaving a portion of the CO_2 phase in an immobile condition (Land C. S., 1971).

The imbibition process becomes important after injection ceases and gravity forces begin to drive CO_2 movement. As CO_2 moves out of a rock volume, brine will flow to fill what the CO_2 "vacated." The residual (i.e., trapped) CO_2 saturation in a simulator grid block will be a function of the maximum trapped gas parameter and the CO_2 saturation at the beginning of the imbibition process (Land C. , 1968). The trapped CO_2 saturation will be at the maximum value for rock volumes in which the liquid saturation was displaced down to its residual value by the CO_2 phase prior to the imbibition.

Typical maximum trapped-gas-saturation parameters range from around 30% to more than 40%. [redacted] A statistical representation of the trapped gas data from Keelan is shown in Figure 2-15. The trapped gas saturation parameter is plotted versus a normal probability function, with horizontal grid lines scaled to represent percentile probability values. In this plot, "P_{90}" represents a value for which 90% of the data will fall below this value. In the scaling of the plot, a straight line represents a normal probability distribution.

In the GEM simulator used to characterize the CO_2 plume movement, the maximum trapped gas saturation parameter was set to [redacted] of the pore volume. This represents a conservative value (i.e., more favorable to the spread of a CO_2 plume) as compared to a median value of [redacted].

Figure 2-15 – Trapped Gas Saturation Experimental Data

The effect of trapped gas was illustrated in Figure 2-2 for Orchard No. 1 (then in Figures 2-4, 2-6, 2-8, 2-10, 2-12, and 2-14 for Orchard No. 2 through No. 7, respectively), where the four panels show how the mobile CO_2 saturations migrate vertically over time. The areas with higher (mobile) saturations of the CO_2 phase are represented by the warmer shades (yellow to red) on the color scale. As the mobile CO_2 moves away from grid blocks, cells are shaded a uniform green, representing saturations at or near the trapped (immobile) saturation of CO_2.

2.2.1.3 Solubility Trapping in Brines

The solubility of [redacted] in the water phase is incorporated into the GEM simulator. The fluid model used Harvey's correlations (Harvey, 1996) for Henry's Law coefficients for the CO_2, nitrogen, and methane components. With the modeled reservoir conditions, brine contacted by the CO_2 phase may have up to 1.9 mole percent of CO_2. This contrasts the trace initial CO_2 saturations (0.008 mole percent) before CO_2 contact. As mobile

CO_2 moves within the reservoir, it will contact "new" brine, which will solubilize additional volumes of CO_2. Additionally, the CO_2-rich water phase has a slightly higher density than the initial water in place, differing by approximately 1%. Over centuries, there may be convective mixing of the water phases, resulting in the solubility trapping of additional moles of CO_2 within the water phase.

2.2.1.4 Solubility Trapping in [redacted]

[redacted] of the pore volume in the top seven simulation layers of the storage interval. These layers are termed the [redacted] The aggregate thickness for these seven layers ranges from around [redacted] thick across the project area, as shown in Table 2-1. The gross injection interval in the current simulation model and the modeled thickness of the ROZ for each of the Orchard injection wells are as follows:

Table 2-1 – Gross Injection Interval and Modeled ROZ Parameters

Well Name	Gross Injection Interval (ft)	Modeled ROZ Thickness (ft)	ROZ Open for Injection (ft)
Orchard No. 1	[redacted]		
Orchard No. 2			
Orchard No. 3			
Orchard No. 4			
Orchard No. 5			
Orchard No. 6			
Orchard No. 7			

[redacted] input into the simulation model as an initial estimate, allowing for characterization of the mechanisms for the trapping of CO_2 [redacted]

Under the right conditions of pressure, temperature, and reservoir oil composition, CO_2 is an attractive injectant for use as a miscible solvent in enhanced oil recovery (EOR) projects. [redacted] The attractiveness of CO_2 as an EOR solvent arises from its high degree of miscibility with the in-place reservoir oil. While not "first contact" miscible, as observed in the mixing of kerosene and gasoline, the CO_2 can achieve complete miscibility through a multi-contact process. This process entails simultaneous evaporation of lighter oil components into the CO_2-rich gas phase along with condensation of CO_2 into the hydrocarbon phase. This process forms a transition phase that is miscible with both the injected CO_2 and in-place oil phases (Stalkup, 1983).

[redacted]

Because of the significant amount of CO_2 contained [redacted] is tracked as the total effective saturation of CO_2—that is, the mole fraction of CO_2 in each of the phases present multiplied by the saturation of the respective phase:

$$S_{CO_2\,e} = S_o \cdot x_{CO_2} + S_g \cdot y_{CO_2} + S_w \cdot w_{CO_2}$$

[redacted]

Figure 2-16 illustrates the comparison of CO_2 phase saturation and the effective total CO_2 saturation at the end of injection and 50 years post-injection for Orchard No. 1. This shows how the effective CO_2 front extends further than does the CO_2-only phase. The difference between the pairs of panels below (image a versus b, and c versus d, respectively) is seen in the shallower layers, where the colors representing CO_2 presence have a larger lateral extent. The primary source of this difference is the CO_2-rich oil phase ahead of the supercritical phase front.

Figures 2-17 through 2-22 then show the same for Orchard No. 2 through No. 7, respectively.

Figure 2-16 – Orchard No. 1 east-west cross-sectional view depicting CO_2 phase versus effective total CO_2.

Figure 2-17 – Orchard No. 2 east-west cross-sectional view depicting CO_2 phase versus effective total CO_2.

Figure 2-18 – Orchard No. 3 east-west cross-sectional view depicting CO_2 phase versus effective total CO_2.

Figure 2-19 – Orchard No. 4 east-west cross-sectional view depicting CO_2 phase versus effective total CO_2.

Figure 2-20 – Orchard No. 5 east-west cross-sectional view depicting CO_2 phase versus effective total CO_2.

Figure 2-21 – Orchard No. 6 east-west cross-sectional view depicting CO_2 phase versus effective total CO_2.

Figure 2-22 – Orchard No. 7 east-west cross-sectional view depicting CO_2 phase versus effective total CO_2.

2.2.1.5 Structural Trapping

Within our area of interest, there is no evidence of structure to trap CO_2. The dip angle through the Orchard Project area is approximately 1.5 degrees, down to the west. (Formation dips were discussed further in *Section 1.4.1*.) The localized near-wellbore dips may affect some slow updip migration of CO_2 plumes; however, because of the gas trapping mechanism, the overall impact of these local dips is small.

2.2.1.6 Geochemical Trapping

Mineral trapping can also occur due to the adsorption of CO_2 onto clay minerals. Once hysteresis and solubility trapping have been included in the model, geochemical formulae can be added through an internal geochemistry database to describe mineral trapping reactions. For aqueous reactions, the following three formulae can be used:

$$CO_2(aq) + H_2O = H^+ + HCO_3^-$$
$$CO_3^{-2} + H^+ = HCO_3^-$$
$$OH^- + H^+ = H_2O$$

Those common ionic reactions can occur in the reservoir between water and/or CO_2. The following formulae show the mineral reactions that may be used within the model. Each of these is a common mineral that may be found in carbonates in an underground aquifer and cause the precipitation of carbon oxides in a solid state:

$$Anhydrite\ (CaSO_4) = Ca^{2+} + SO_4^{2-}$$
$$Calcite\ (CaCO_3) + H^+ = Ca^{2+} + HCO_3^-$$
$$Dolomite\ (CaMg(CO_3)_2) + 2H^+ = Ca^{2+} + 2(HCO_3^-) + Mg^{2+}$$
$$Illite\ (K_6Mg_{25}Al_{2.3}Si_{3.5}O_{10}(OH)_2) + 8H^+ = 2.3Al^{3+} + 5H_2O + 0.6K^+ + 0.25Mg^{2+} + 3.5SiO_2$$
$$Kaolinite\ \left(Al_2Si_2O_5(OH_4)\right) + 6H^+ = 5H_2O + 2Al^{3+} + 2SiO_2$$
$$K - Feldspar\ (KAlSi_3O_8) + 4H^+ = 2H_2O + Al^{3+} + 3SiO_2$$

While geochemical trapping can have a greater impact on carbon dioxide over hundreds or thousands of years, the short-term effects of these trapping mechanisms are relatively small (i.e., not significant), and fluid movement is predominated by hydrodynamic and solubility trapping. Given that, plus the significant computational burden on the model runs created by including geochemical reactions and trapping mechanisms in the GEM simulator, the geochemical processes have not been included in the simulation cases.

2.2.1.7 Trapping Summary

After the containment zone overlying the reservoir, the significant mechanisms by which CO_2 is trapped in the storage interval are illustrated in Figure 2-23, which also shows the metric tons of injected CO_2 in the mobile phase and in each of the trapped phases. In this and the figures following, "rel perm" refers to relative permeability.

Figure 2-23 – Balance of Injected CO_2

2.2.2 Structural and Stratigraphic Elements

The model was built using the geologic data described in *Section 1 – Site Characterization*, on how the analysis of well logs, core data, and seismic data were used to generate structure maps and hydrogeology, and to define other rock properties. Specifically, *Section 1.3.2* discussed the stratigraphy of the modeled injection zone. The simulation model was built for the approximately

Figure 2-24 – Horizontal Permeability at Orchard No. 1 Injector (East-West Section)

Figure 2-25 – Horizontal Permeability at Orchard No. 2 Injector (East-West Section)

Figure 2-26 – Horizontal Permeability at Orchard No. 3 Injector (East-West Section)

Figure 2-27 – Horizontal Permeability at Orchard No. 4 Injector (East-West Section)

Figure 2-28 – Horizontal Permeability at Orchard No. 5 Injector (East-West Section)

Figure 2-29 – Horizontal Permeability at Orchard No. 6 Injector (East-West Section)

Figure 2-30 – Horizontal Permeability at Orchard No. 7 Injector (East-West Section)

Tables 2-2 through 2-8 summarize the values for porosity and permeability for injection zone model layers at the Orchard No. 1 through No. 7 locations, respectively.

Table 2-2 – Orchard No. 1 Model Porosity and Permeability Summary

		Porosity	Perm (mD)
[redacted]			

Table 2-3 – Orchard No. 2 Model Porosity and Permeability Summary

		Porosity	Perm (mD)
[redacted]			

[redacted]

Table 2-4 – Orchard Well No. 3 Model Porosity and Permeability Summary

		Porosity	Perm (mD)
[redacted]			

Table 2-5 – Orchard No. 4 Model Porosity and Permeability Summary

		Porosity	Perm (mD)
[redacted]			

Table 2-6 – Orchard No. 5 Model Porosity and Permeability Summary

		Porosity	Perm (mD)
[redacted]			

Table 2-7 – Orchard No. 6 Model Porosity and Permeability Summary

		Porosity	Perm (mD)
[redacted]			

Table 2-8 – Orchard No. 7 Model Porosity and Permeability Summary

		Porosity	Perm (mD)
[redacted]			

Vertical Permeability

Permeability normal to the bedding plane is usually lower than the permeability in the parallel direction. In most cases, "normal to the bedding plane" equates to *vertical* permeability, while the parallel-direction permeability corresponds to *horizontal* permeability. This contrast is caused by vertical heterogeneity over multiple scales, from very small (fractional inch) through many feet in range. By comparison, the scales of heterogeneity in the horizontal orientation will be significantly larger.

When permeabilities are averaged for upscaling into the simulator grid cell scale, flow in the direction normal to the heterogeneity will be significantly affected by the lowest permeability layers. For this reason, vertical permeability is typically characterized by the harmonic mean of layer permeabilities. In contrast, the horizontal flow (within the model) is typically characterized by the higher arithmetic mean value for permeability. Ratios of vertical to horizontal permeability (k_v/k_h) in the range of 0.01 to 0.05 are very common in history-matched simulations of hydrocarbon fields. In the Orchard simulator model, a value of 0.03 was chosen. This can be considered as a moderate vertical permeability ratio.

While the k_v/k_h ratio of 0.03 may seem low, the flow between simulator grid blocks—and in the physical world—is controlled by transmissibility rather than permeability alone. For constant viscosity and relative permeability, the transmissibility can be represented by the equation $T = \frac{k \times A}{L}$, where A is the cross-sectional area to flow and L is the length over which the flow (e.g., grid block

center to center) travels. For simulator grid-cell dimensions, vertical flow between grid cells has a large area and small distance, while the horizontal flow between cells has a relatively large distance across a (relatively) small cross-sectional area. In the Orchard simulation model, typical grid blocks are 492 ft x 492 ft (150 meters square) by 20 ft thick. The vertical A/L term will therefore be 600 times larger than the horizontal term. With a k_v/k_h ratio of 0.03, vertical transmissibility is still nearly 20 times higher than the horizontal transmissibility.

2.2.3 Relative Permeability and Capillary Pressure

Relative permeability curves were generated using the industry-standard power law model based on the approach developed by Corey (Corey, 1954). In this model, the relative permeability for the respective water and supercritical gas phases are based on the normalized saturation, scaled between the end points of mobility for a respective phase, and raised to an exponent value (termed the "Corey exponent"). Relationships for water and gas relative permeabilities can be expressed with the following equation. The gas relative permeability applies to the supercritical CO_2 phase.

$$k_{rw} = k_{rwcg} \left[\frac{(S_w - S_{wc})}{(1 - S_{wc} - S_{gc})} \right]^{nw}$$

And

$$k_{rg} = k_{rgrl} \left[\frac{(S_g - S_{gc})}{(1 - S_{wc} - S_{gc})} \right]^{ng}$$

Where:

k_{rw}, k_{rg} = Relative permeability to water and gas phases, respectively

k_{rwcg} = Water relative permeability endpoint, k_{rw} at critical gas saturation

k_{rgrl} = Gas relative permeability endpoint, k_{rc} at irreducible water saturation

S_w, S_g = Water and gas saturations, respectively

S_{wc} = Irreducible saturation of water

S_{gc} = Critical saturation of gas

nw, ng = Corey exponents for water and gas curves, respectively.

Figure 2-31 shows the gas-liquid relative permeability curves for the drainage process (CO_2 displacing water) used in the reservoir simulation model. These curves were generated using "generic" Corey exponents of 2.0 for both the liquid and supercritical gas phases.

Figure 2-31 – Gas-Liquid Relative Permeability Relationship

The red curve shows the relative permeability to the supercritical CO_2 phase, starting at a maximum value of [redacted] and decreasing with increasing liquid saturations. The liquid-phase relative permeability is shown as the blue curve, starting at zero at the irreducible liquid saturation value of [redacted] and increasing together with the liquid saturation.

The value of [redacted] for the CO_2 phase relative-permeability endpoint may be considered low relative to "conventional" relative-permeability data used in the energy industry. [redacted] Figure 2-32 shows a statistical distribution of the CO_2 endpoint relative-permeability data for carbonates, taken from the [redacted] papers as well as the National Energy Technology Laboratory's CO_2 Brine Relative Permeability Database (NETL-CO2BRA) (Crandall, Moore, Brown, & King, 2019). On this plot, data values are plotted on the horizontal axis against the standard deviation for that data vs. the entire distribution. Horizontal lines are the probability (analogous to "percentile") for the data within the distribution. Data that lie in a straight line when plotted on a logarithmic scale for the horizontal axis, as Figure 2-32 indicates, denote a log-normal distribution.

Figure 2-32 – Probability Distribution of CO_2 Endpoint Relative Permeability

When considering a relative permeability relationship, it is important to look at the data in the context of reservoir conditions, using in situ fluid properties by the generation of a fractional flow curve. Absent gravity effects, the fractional flow of CO_2 vs. saturation is calculated using the relationship:

$$f_g = \frac{1}{1 + \frac{\mu_g}{\mu_w}\frac{k_{rw}}{k_{rg}}}$$

Where f_g represents the volume fraction of the gas (supercritical CO_2), μ_g and μ_w represent the in-situ viscosity for the CO_2 and brine, and k_{rw} and k_{rg} represent the relative permeability for the brine and CO_2 at the saturations evaluated. Figure 2-33 shows the fractional flow curve for CO_2 arising from the relative permeability curve, together with in situ fluid viscosities.

This plot includes a tangent line according to Welge's method for analysis of Buckley-Leverett displacement theory (Buckley & Leverett, 1942) (Welge, 1952). Taken together, the fractional flow curve and its "Welge Tangent" will indicate that the displacement of water by CO_2 will be relatively efficient, having a nearly "piston-like" behavior. In a volume of rock with 1D flow (e.g., a core plug), the brine will be displaced by the CO_2 phase ahead of a fluid front, often termed a "shock front." Phase saturations are not continuous. Ahead of the displacing fluid front, the rock volume will be at 100% brine saturation. According to Welge, the tangent point saturation (0.36) defines the CO_2

phase saturation at the front, while the extrapolation of the tangent line to 1 will indicate the average CO_2 saturation [redacted] behind the shock front. These 1D-displacement analysis results predict that the displacement of water by CO_2 will be efficient, leading to compact CO_2 plumes having relatively high CO_2 saturations behind the plume front. This behavior can be confirmed from the simulation results that Figure 2-16 displayed (for Orchard No. 1, with similar figures there following for Orchard No. 2 through No. 7 respectively, in *Section 2.2.1.4*).

Figure 2-33 – CO_2 Fractional Flow Curve

The displacement and relative permeability curves represent the displacement of water by injected CO_2. In the reverse process, discussed in *Section 2.2.1.2*, formation brine replaces CO_2 that flows out of the rock volume; the CO_2 will not return to its initial saturation, but rather leave behind a trapped gas saturation.

2.2.3.1 Capillary Pressure Relations

Capillary pressure relations were not incorporated into the simulation model. The effects of capillary pressure are implicit in the no-flow nature of the upper and lower confining beds. Low permeabilities, together with associated high capillary-entry pressures, will combine to prevent flow through the confining interval. Within the [redacted] itself, the incorporation of capillary pressure into the model is not expected to be significant, and certainly would not increase rates of

plume growth. Capillary entry pressures at lower permeability "baffles" would likely slow migration of CO_2 into those cells.

2.2.4 Initial Conditions

[redacted] as Table 2-9 shows.

Table 2-9 – Reservoir Pressure Gradient Data for Nearby [redacted]

Field	San Andres Reservoir Pressure Gradient
[redacted]	

The formation temperature in the simulation model was initialized to a constant temperature of 105°F. This is based on bottomhole temperature data reported on well-log headers for several nearby wells and provided in Table 2-10. Temperature gradients were calculated from an estimated surface soil temperature of 65°F.

Table 2-10 – Formation Temperature for Orchard Area Wells

Well ID No.	Maximum Temperature (°F)	Depth (ft)	Calculated Gradient (°F/100 ft)
[redacted]			

The temperature gradient data are used with the surface temperature from which they were derived (65°F) to determine a formation temperature at depth.

The gradient data are then presented in Figure 2-34, which yields a median temperature gradient for the Orchard Project area of [redacted]. Incorporating that median gradient with a formation datum depth approximately [redacted] below surface yields a temperature of [redacted] That was increased to [redacted] to reflect the suppression of measured wellbore temperatures due to mud circulation [redacted]

Figure 2-34 – Orchard Area Temperature Gradients

The EOS fluid property model used in this simulation model is summarized in *Appendix 2-2*.

, the storage interval is essentially brine filled, with trace amounts of hydrocarbon present. This inclusion of trace volumes of hydrocarbons significantly helps the computational stability for the GEM simulator. Dissolved solids content for the formation brine was set to parts per million (ppm). This value was chosen as the median dissolved solids for water samples in and around the Orchard area, as plotted in Figure 2-35.

The principal impact of total dissolved solids (TDS) present will affect the density of the formation brine and its ability to dissolve CO_2. Density of the formation brine has been calculated using correlations of McCain (see *Appendix 2-1*) to be pounds per cubic foot (lb/ft^3), yielding a gradient of 0.448 psi/foot at downhole conditions.

Figure 2-35 – Normal Probability Plot of Gaines County TDS Data in the San Andres Formation

2.2.5 Injection Rate

Injection rates are controlled in the simulator by the overall injection target rate and individual well injectivity. Each well will inject at its allocated rate, subject to a maximum bottomhole injection pressure limit. The maximum injection pressure is calculated based on the measured depth of the shallowest open layer into which each well is injecting, using a gradient of [redacted] The limiting pressure gradient will be updated to 90% of the fracture gradient, when measured with the step-rate test.

The overall project injection target was set to 121.5 million standard cubic feet per day (MMscf/d), which corresponds to the project target rate of 2.3 million metric tons per year (MMT/yr) of CO_2 for an inlet stream with 98% purity, converted at standard conditions of 14.7 pounds per square inch absolute (psia) and 60°F. The range of proposed injection for the seven Orchard Project wells, detailed in *Section 3.3* (Table 3-1), [redacted] While there are injection pressure limits set for each well, sufficient spare capacity exists for all wells to operate at

bottomhole pressures below their limits. In this case, where there is spare capacity available to the model, the simulator internally allocates injection rates based on the calculated injectivity for each of the injection wells.

2.2.6 Injected Fluids Composition

While the simulation model was constructed with a nine-component EOS to describe the fluids found in the [redacted] the injected fluid composition was simplified to include two components, CO_2 and N_2. This composition was set to be 98% CO_2 and 2% N_2 for model simulations prior to collection of actual compositional data. The nitrogen impurity was chosen to create a characterization for an injected fluid with a relatively soluble element (CO_2) combined with a relatively insoluble impurity (N_2). These solubility characteristics apply to dissolution in both water- and hydrocarbon-phase liquids.

The exact injected-fluid composition will depend on the average compositions over time within the [redacted] The value of 98% CO_2 was chosen as a mid-range placeholder between the minimum specification and pure CO_2. This composition will be adjusted as pipeline compositional data becomes available.

2.2.7 Completion Plan

The proposed Orchard No. No. injection wells will be perforated and stimulated in all permeable layers through the [redacted] (i.e., injection interval). This is simulated in the model by opening layers with permeabilities greater than 1.5 millidarcys (mD) based on the petrophysical evaluation. This completion strategy will be implemented for all the injectors planned in the Orchard Project. Actual model perforation selection was done based on a qualitative inspection of permeabilities at each well location. The interval and timing inputs to the model for the injection wells are shown in Table 2-11. Figures 2-36 through 2-42 show a cross-sectional view of grid block permeability at the Orchard No. 1–No. 7 well locations, respectively. In each, the "perforated" grid blocks are flagged on the wellbore diagrams with green circles.

Table 2-11 – Orchard No. 1–No. 7 Model Completion Timing

Injection Well	Year	Duration	Top (ft)	Thickness (ft)	Net Pay (ft)	Geologic Layer
[redacted]						

[redacted]

[redacted]

Figure 2-36 – Orchard No. 1 Perforations

[redacted]

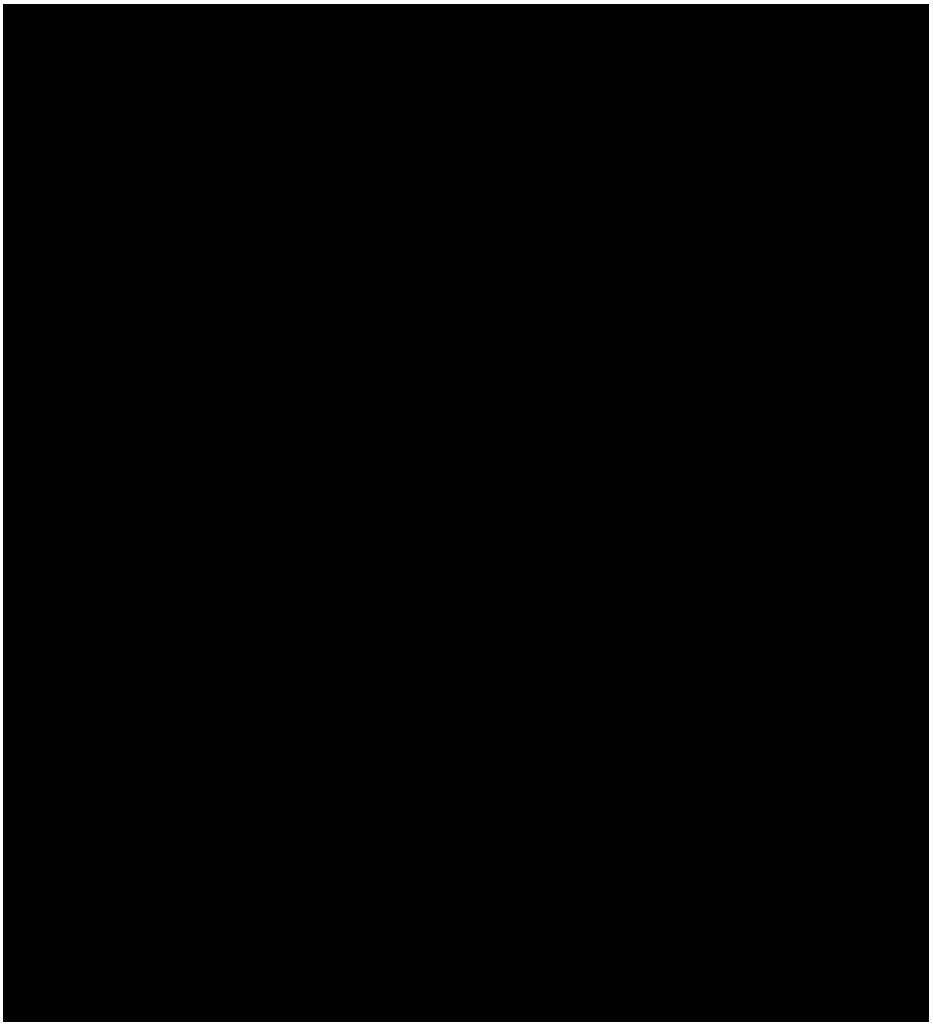

Figure 2-37 – Orchard No. 2 Perforations

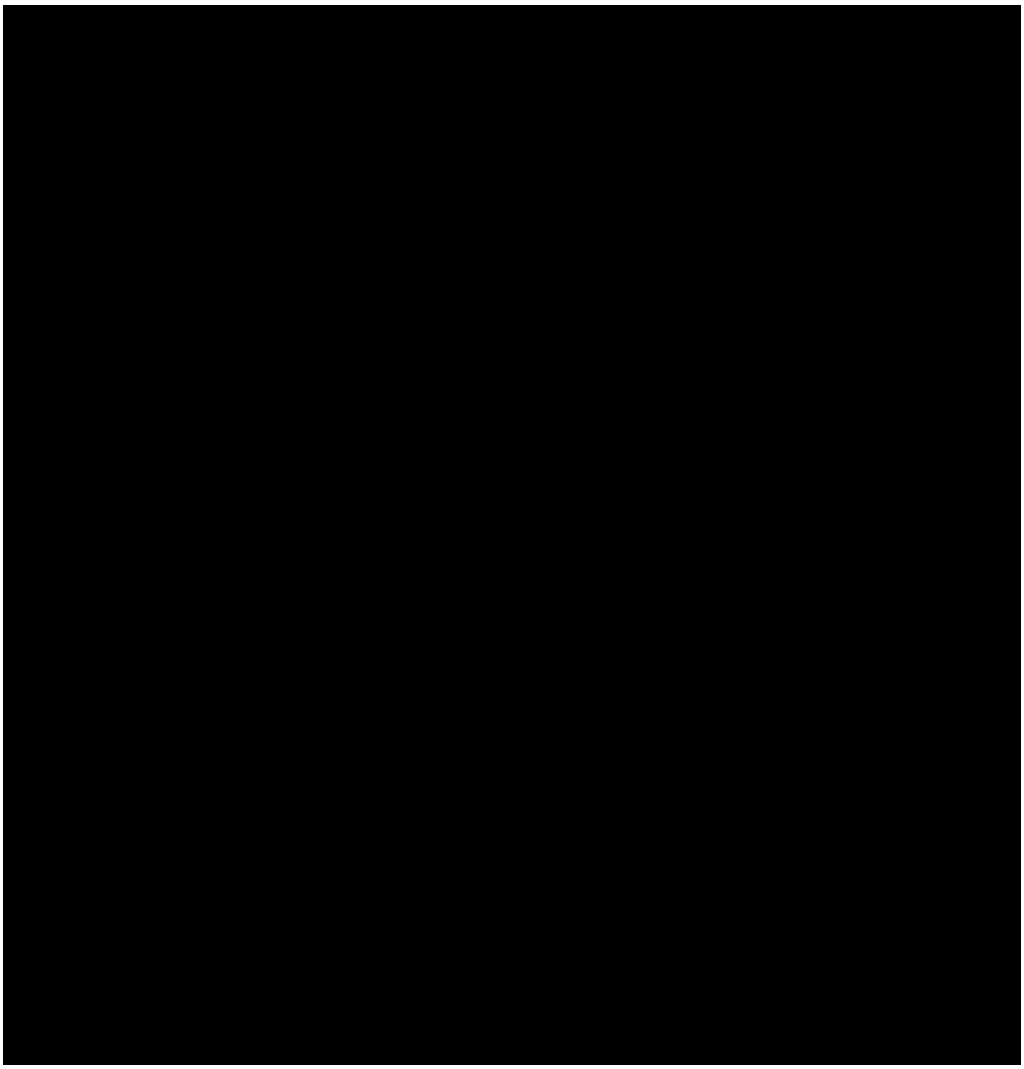

Figure 2-38 – Orchard No. 3 Perforations

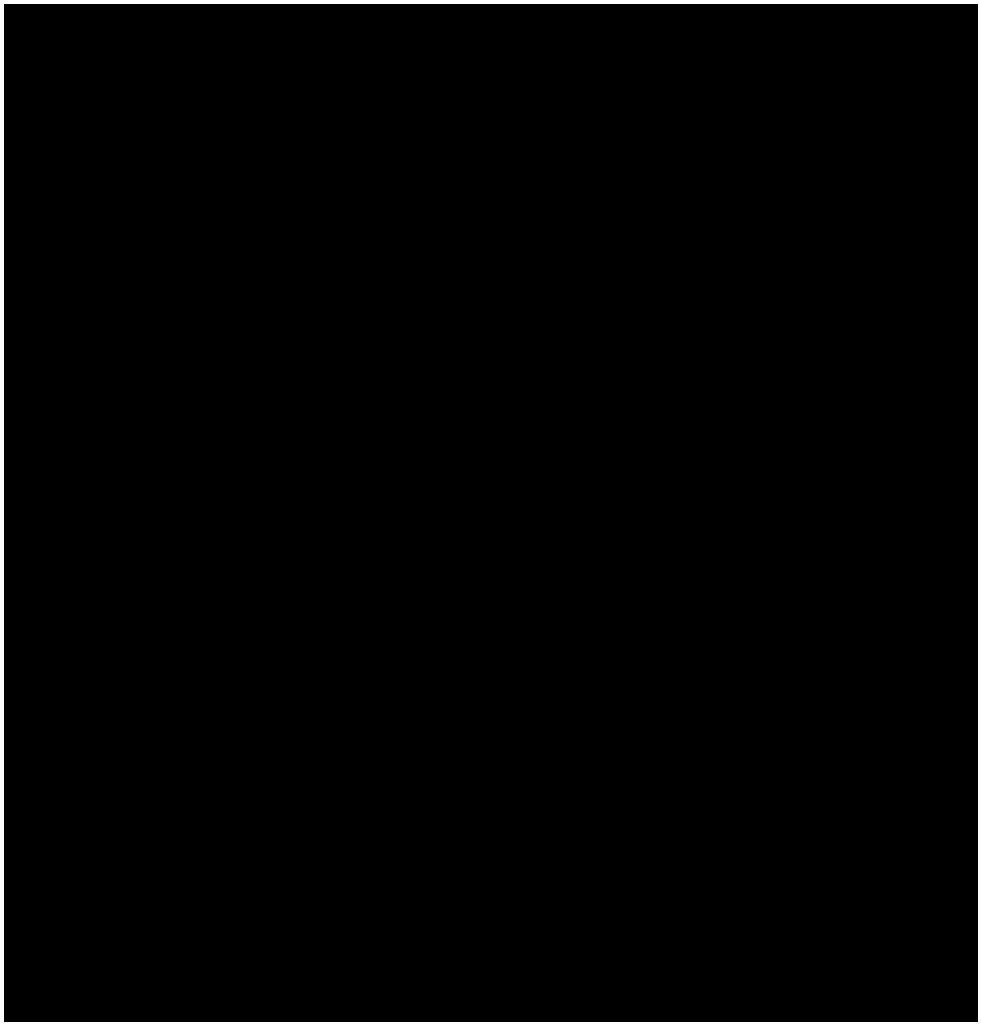

Figure 2-39 – Orchard No. 4 Perforations

Figure 2-40 – Orchard No. 5 Perforations

Figure 2-41 – Orchard No. 6 Perforations

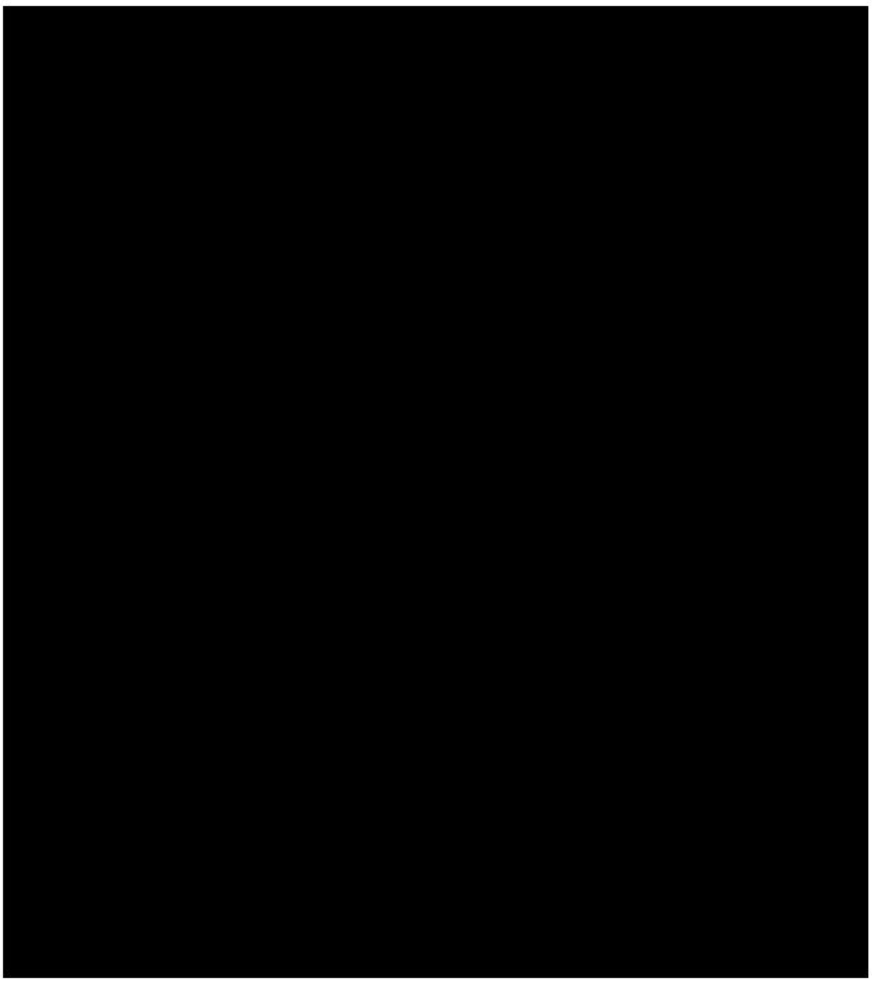

Figure 2-42 – Orchard No. 7 Perforations

The stimulation aspect of the completion strategy was modeled by assigning a skin value of -3.5 to all wells upon initial completion. This skin value corresponds to a small fracture stimulation with a half-length around 25 ft. In addition to improving injectivity in each well, the strategy of stimulating the formations ensures that all perforated intervals are open, to better manage vertical injection conformance.

2.3 Model Orientation and Gridding Parameters

2.3.1 Spatial Conditions

The simulation of the CO_2 injection and migration was performed for the [redacted] Figure 2-36 through Figure 2-42 (*Section 2.2.2*) showed a representation of permeability near the planned injection wells. No.

The reservoir simulator covers [redacted] The model gridding is proportional (i.e., layers in each of the respective zones are of equal thickness).

The overall active model area consists of 170 x 140 x 61 grid blocks in the x, y, and z dimensions, respectively. Block x and y dimensions are a constant 150 meters (492 ft). The model covers an area of 15.9 x 13.1 miles (east-west and north-south, respectively), with a total area of 246 square miles—that is, 1.45 million active grid blocks. Grid block thicknesses vary throughout the model, as shown in Table 2-12. Boundary conditions are described in *Section 2.3.2*.

Table 2-12 – Model Layer Parameters

Well Name	[redacted]
Orchard No. 1	
Orchard No. 2	
Orchard No. 3	
Orchard No. 4	
Orchard No. 5	
Orchard No. 6	
Orchard No. 7	

The vertical variation in permeability throughout the simulator area is considerable, with values ranging from a minimum of 0.001 mD up to a maximum of more than [redacted]. Tables 2-13 through 2-19 illustrate the ranges of permeabilities in the injection interval around each of the Orchard No.–No. 7 injection wells (11 x 11 grid cells x-y, approximately 1 square mile).

Table 2-13 – Simulator Permeability Values in Area of Orchard No. 1 Well

	Average Permeability (mD)	Minimum Permeability (mD)	Maximum Permeability (mD)
[redacted]			

Table 2-14 – Simulator Permeability Values in Area of Orchard No. 2 Well

	Average Permeability (mD)	Minimum Permeability (mD)	Maximum Permeability (mD)
[redacted]			

Table 2-15 – Simulator Permeability Values in Area of Orchard No. 3 Well

	Average Permeability (mD)	Minimum Permeability (mD)	Maximum Permeability (mD)
[redacted]			

Table 2-16 – Simulator Permeability Values in Area of Orchard No. 4 Well

	Average Permeability (mD)	Minimum Permeability (mD)	Maximum Permeability (mD)
[redacted]			

Table 2-17 – Simulator Permeability Values in Area of Orchard No. 5 Well

	Average Permeability (mD)	Minimum Permeability (mD)	Maximum Permeability (mD)
[redacted]			

Table 2-18 – Simulator Permeability Values in Area of Orchard No. 6 Well

	Average Permeability (mD)	Minimum Permeability (mD)	Maximum Permeability (mD)
[redacted]			

Table 2-19 – Simulator Permeability Values in Area of Orchard No. 7 Well

	Average Permeability (mD)	Minimum Permeability (mD)	Maximum Permeability (mD)
[redacted]			

The distribution of cumulative injection [redacted] injection interval. Also notable is the wide range between minimum and maximum permeabilities in Table 2-13 through 2-19. A more useful measure of heterogeneity would be to look at the ratio of 10th to 90th percentile values. Comparing that ratio for permeability within individual layers to the entire volume provides insight into the relative amounts of heterogeneity in the vertical vs. horizontal directions. Table 2-20 shows ratios of 90th to 10th percentile values for permeability in the [redacted] injection intervals for all seven injection wells. The first column shows the ratio for the entire volume centered on each of Orchard No. No. injection wells, while the second shows the average of that ratio for data populations by layer. This table illustrates that, within the Orchard No. Project area, the lateral variation of permeability is approximately one order of magnitude less than the overall variation, which is dominated by vertical heterogeneity.

Table 2-20 – Comparison of Statistical Measures for Permeability for Orchard No. 1–No. 7

Zone	P_{90} / P_{10} ratio – entire volume	P_{90} / P_{10} ratio – average of layer values
[redacted]		

From a wellbore injectivity perspective, the wells penetrate many layers that would be considered "non-pay" due to relatively low permeabilities. These non-pay intervals are important in the reservoir simulation model, as even the low-permeability grid cells provide significant pore-volume compressibility to the model.

2.3.2 Boundary Conditions

Boundary Definition

The top and base of the model were set up as no-flow boundaries to vertical flow, these being the upper and lower confining zones, respectively. Each of the lateral edges of the model has been connected to one or more numerical aquifers, using the Fetkovich water-influx calculation option (Fetkovich, 1971), to characterize connections between the modeled area and surrounding region. The use of Fetkovich-type numerical aquifers allows for the definition of aquifers having finite connectivity to the reservoir model. In this setup, bounding aquifers on the north, west, and south simulation boundaries are very large and effectively infinite. [redacted] Analysis of the early

performance data is discussed in *Section 2.3.2.1*. [redacted]

The Fetkovich method uses an aquifer productivity index—or, in this case, an injectivity index parameter with units of reservoir barrels per day per psi. This parameter is defined in the simulator based on reservoir properties (thickness, permeability) on the model face and the size of the aquifer: $effective\ {}^{r_a}/_{r_r}$, equivalent to an ${}^{r_e}/_{r_w}$ term in the radial flow equation, where "r_a" refers to the effective outer radius of the aquifer, and "r_r" refers to the effective outer radius of the reservoir simulator.

As a result of this definition of the boundaries, the model is connected to large regional reservoir volumes on three sides, with transmissibility between the simulator and aquifer volumes based on average permeabilities on each respective face. Connectivity to the east side is also based on the permeabilities on that face. However, the reservoir volume, though substantial (12 x 10^9 reservoir barrels), only amounts to 7% of the pore volume contained by the active reservoir simulation grid.

2.3.2.1 [redacted] This study includes a description of the initial reservoir oil in place ("PVT data"), as well as a plot of reservoir pressure vs. time during early production. The PVT data shows that the reservoir oil was initially very undersaturated, having a bubble point pressure of 326 psia. The pressure data plot indicates that the [redacted] reservoir pressures stayed above the bubble point during early production, [redacted]. The combination of good reservoir pressure data with depletion above the bubble point indicates that simple material balance calculations are appropriate and effective. These calculations are used to estimate connected in-place volumes of reservoir fluids and the potential for aquifer pressure support.

Given the pressure decline above the bubble point for [redacted], the early production mechanism lends itself to the simplest form of material balance. Absent external water influx, fluid withdrawals from such a reservoir will affect a decline in pressure, controlled by three terms. These terms, affected by changes in reservoir pressure, will be (1) the reduction in pore volume, (2) expansion of connate water, and (3) expansion of reservoir oil. A description of the case for fluid expansion above the bubble point is described in the referenced text (Craft & Hawkins, 1959).

Using the parameters for the [redacted] tabulated in Table 2-21, a match to the pressure decline vs. cumulative production (Figure 2-43) was obtained for an oil-in-place (OIP) estimate of [redacted]

Table 2-21 – [redacted] Reservoir Parameters

Parameter	Value
Initial Reservoir Pressure (psi)	[redacted]
Initial Water Saturation (%)	
Initial Oil Formation Volume Factor (RB/STB*)	
Oil Compressibility (psi^{-1})	
Water Compressibility (psi^{-1})	
Formation Compressibility (psi^{-1})	

*Reservoir barrel per stock-tank barrel.

Figure 2-43 – [redacted] Material Balance

The results of the material-balance match are significant when considering the regional connectivity of the [redacted] If the field was connected to a much larger pore volume (i.e., a regional aquifer), the material balance should reflect very large pore volumes. This evaluation, however, indicates that [redacted] is likely not in communication with the surrounding area, particularly the Orchard Project area. The data acquired during the drilling of the well will confirm this analysis. [redacted] currently operates at higher than initial pressures, approximately [redacted] Contrary to the performance-based evidence

described above [redacted]

2.3.3 Model Time Frame

The reservoir simulation model was run for a period of [redacted] During the latter (i.e., non-injecting) phase, the movement of the CO_2 phase is a largely gravity-driven vertical migration as discussed in *Section 2.2.1*. Figure 2-44 shows a graph of the aggregate plume size for the seven injectors over time. The plume size is calculated based on the maximum value of effective CO_2 saturation through all layers at any x, y (or model "I, J") map location, with saturations above a 3% minimum value as a cutoff. The calculation of effective CO_2 content was described in *Section 2.2.1.4.*

Figure 2-44 – Aggregate Plume Growth Vs. Time for Orchard Project Injection Wells

The horizontal axis on this plot is *years*, referenced to the end of the injection period. The figure shows how the plume stabilizes to a very slow growth rate within the first few years post-injection.

2.4 CO_2 Plume Model Results

Model cases were run that included all wells, to ensure overall injectivity while honoring injection pressure limits. Figure 2-45 shows the stabilized CO_2 plumes for all seven injection wells at 50 years post-injection. Figures 2-46 through 2-59 display cross sections of the CO_2 plumes for Orchard No. 1–No. 7, respectively, taken at the end of injection and 50 years post-injection.

Figure 2-45 – Stabilized CO_2 Plumes, 50 Years Post-Injection

Figure 2-46 – Orchard No. 1 East-West Cross-Sectional Views of Effective CO_2 Saturation

Figure 2-47 – Orchard No. 1 North-South Cross-Sectional Views of Effective CO_2 Saturation

Figure 2-48 – Orchard No. 2 East-West Cross-Sectional Views of Effective CO_2 Saturation

Figure 2-49 – Orchard No. 2 North-South Cross-Sectional Views of Effective CO_2 Saturation

Figure 2-50 – Orchard No. 3 East-West Cross-Sectional Views of Effective CO_2 Saturation

Figure 2-51 – Orchard No. 3 North-South Cross-Sectional Views of Effective CO_2 Saturation

Figure 2-52 – Orchard No. 4 East-West Cross-Sectional Views of Effective CO_2 Saturation

Figure 2-53 – Orchard No. 4 North-South Cross-Sectional Views of Effective CO_2 Saturation

Figure 2-54 – Orchard No. 5 East-West Cross-Sectional Views of Effective CO_2 Saturation

Figure 2-55 – Orchard No. 5 North-South Cross-Sectional Views of Effective CO_2 Saturation

Figure 2-56 – Orchard No. 6 East-West Cross-Sectional Views of Effective CO_2 Saturation

Figure 2-57 – Orchard No. 6 North-South Cross-Sectional Views of Effective CO_2 Saturation

Figure 2-58 – Orchard No. 7 East-West Cross-Sectional Views of Effective CO_2 Saturation

Figure 2-59 – Orchard No. 7 North-South Cross-Sectional Views of Effective CO_2 Saturation

Figure 2-44 demonstrated how the plume areal extent stabilizes during the first few years post-injection. While the plume areas quickly stabilize, the trapping of the CO_2 phase progresses over many years (discussed in *Section 2.2.1.7*). Figures 2-60 and 2-61 show how the trapped CO_2 volumes will change over time for the Orchard Project.

Figure 2-60 – Total Metric Tons of CO_2 and Trapping Mechanisms Over Time

Figure 2-61 – Percent of CO_2 in Each State Over Time

2.4.1 Critical Pressure Front

The second component to defining the AOR is determining the extent of the critical pressure front. The worst-case scenario for moving reservoir fluids to the Underground Source of Drinking Water (USDW) would be through either an improperly plugged and abandoned wellbore, or a subsurface feature that is open in the base of the USDW and at the top of the injection interval. This resultant pressure is referred to as the *critical pressure*. The methodology for finding critical pressure was sourced from Environmental Protection Agency (EPA) Method 1 guidance, for calculations based on displacing fluid initially present in the borehole in the hydrostatic case.

The base of the USDW is expected to be at [redacted] above sea level as observed on offset data from API No. [redacted] Critical pressure is calculated at the top perforated interval for the Orchard No. 6 well, which represents the shallowest perforation top of all seven of the Orchard injectors.

The fluid in the injection zone is assumed to be brine with [redacted] of TDS, based on data from the U.S. Geological Survey's National Produced Waters Geochemical Database, taken for wells close

to the Orchard Project area (and distributed as displayed in Figure 2-43, in *Section 2.3.2.1*). The density of the formation brine in the injection zone was calculated to be [redacted], using correlations by McCain (McCain, 1991). The fluid gradient within the storage interval will therefore be [redacted]

The USDW intervals have been split into two segments—one shallow, one deep—to calculate the pressure at the base USDW. The shallower segment consists of the primary Ogallala aquifer and the underlying secondary Edwards-Trinity (High Plains) aquifer, intervals that Orchard-area water wells currently use. Average TDS values for those two aquifers are [redacted] respectively, yielding a fluid gradient of [redacted] psi per foot for both. The estimated thickness of this shallower segment is [redacted] based on drillers' logs from the [redacted] water wells.

Properties for the USDW segment *below* the Ogallala are based on known data for the Dockum group, which underlies the Ogallala. This deeper segment is known to have significantly higher TDS than that found in the Ogallala. [redacted] The density value derived using McCain yields a pressure gradient of 0.434 psi/foot. (*Appendix 2-1* discusses the McCain correlation.)

To calculate the pressure at the base of the USDW, the hydraulic head was determined in the Ogallala aquifer (i.e., shallow segment). The Texas Water Development Board's (TWDB) database of groundwater source wells in Texas contains information for wells in which liquid levels are routinely measured. Currently designated as Groundwater Conservation District (GCD) observation wells by the TWDB, four of such wells were found within the Orchard AOR and have good quality data from late 2021 and 2022. Table 2-20, which lists those wells, presents their elevations of water level (i.e., the hydraulic head in Ogallala) and date of measurement.

Table 2-22 – Ogallala Aquifer GCD Observation Well Data

Water Well No.	Water Level (Feet Above Sea Level)	Measurement Date
[redacted]		

From this data, water well [redacted] has the deepest liquid level, at an elevation of [redacted] t above sea level. Using that ground-level elevation and a thickness of [redacted] t for the shallower segment, the following input parameters were used to calculate critical pressure, tabulated in Table 2-21. For brevity in the table, the shallow segment (Ogallala and Edwards – Trinity (High Plains) aquifers) is termed "Ogallala."

Table 2-23 – Inputs for Critical Pressure Calculation (Subsea Elevations)

Input Variable	Value
Hydraulic head elevation of Ogallala aquifer (ft)	[redacted]
Fluid gradient in Ogallala aquifer (psi/ft)	
Base Ogallala elevation (ft)	
Hydrostatic pressure differential in Ogallala (psi)	
Calculated pressure at base of Ogallala (psia)	
USDW fluid gradient below Ogallala (psi/ft)	
Fluid column below Ogallala (ft)	
Hydrostatic pressure differential in lower USDW segment (psi)	
Initial fluid pressure at the base of USDW (P_u) – (psia)	
Injection zone pressure gradient ($\rho_i g$)	
Representative elevation of USDW (z_u) – (ft)	
Representative elevation of injection zone (z_i) – (ft)	

The pressure at the base of the USDW (P_u) was calculated in two steps. First, for the column of fresh water in the Ogallala, P_O was calculated at its base:

(Eq. 1) $\Delta P_O = \rho g \cdot (z_h - z_O)$ [redacted]

Where z_h and z_o represent the respective elevations for the top of the water column and base of the Ogallala aquifer. Pressures have been converted to absolute pressure for consistency with pressures calculated within the plume simulation model.

Second, to arrive at the pressure at the base USDW (P_u), a similar calculation was employed:

(Eq. 2) $P_u = P_O + \rho g \cdot (z_O - z_u)$ [redacted]

Where z_u is the representative elevation of the USDW.

Representative elevation and pressure for the injection zone was chosen from Orchard No. 6, which has the shallowest injection interval of the seven Orchard injectors. Elevation (z_i) for the shallowest injection in Orchard No. 6 is at [redacted]. Pressure at that elevation (P_i) is calculated by correcting the simulator initial pressure ([redacted] at datum elevation of [redacted] to the depth of the shallowest injection zone, using the pressure gradient of [redacted] psi per foot:

(Eq. 3) [redacted]

The pressure front ($P_{i,f}$) calculations for the injection zone are:

(Eq. 4) $P_{i,f} = P_u + \rho_i g \cdot (z_u - z_i)$

Where P_u is the initial fluid pressure in the USDW, ρ_i is the injection-zone fluid density, g is the acceleration due to gravity, z_u is the representative elevation of the USDW, and z_i is the representative elevation of the injection zone.

The critical pressure rise ($\Delta P_{i,f}$) is then calculated:

(Eq. 4) $\Delta P_{i,f} = P_u + \rho_i g \cdot (z_u - z_i) - P_i$ [redacted]

The resulting rise in critical pressure for the uppermost stage is positive, indicating that the reservoir pressure may be safely increased by [redacted] psi without risk of fluid migration to the USDW.

The expected pressure differential relative to pre-injection pressures for each of the Orchard No. No. injection wells is presented in Figures 2-62 through 2-68, respectively. The differential pressure, calculated for each grid block in the simulation model, is a snapshot of the difference between the pressure prior to the start of injection and the pressure at a given time post-injection. The data plotted on the graph represent the maximum for that differential pressure for all simulator grid blocks penetrated by each of the Orchard injectors.

Figures 2-62 through 2-68 also present the maximum differential pressure (Δp) vs. time, plotted as circles, for each injector. The horizontal axis represents time in years, relative to the start of injection. The vertical axis represents the maximum Δp value in psi. The dashed horizontal line shows the value of the critical pressure differential calculated at [redacted] psi, and a vertical dashed line flags the time at which injection ceases for this project.

The dominant mechanisms for CO_2 flow in the storage interval will change over time (discussed in *Section 2.2.1*). Likewise, the values and location for the maximum differential pressure will be controlled by different mechanisms over the life of the project. During injection, the highest Δp values are dominated by the horizontal flow away from the wellbore in the more permeable layers. These are the layers into which the majority of CO_2 is injected. The maximum Δp values increase with time until injection ends [redacted]. While the storage interval is effectively infinite-acting, pressures near the wellbore will increase with continued injection due to transient pressure effects, as the effective radius influenced by the injection pressure expands with continued injection.

Figure 2-62 – Orchard No. 1 Maximum Pressure Buildup of All Layers

Figure 2-63 – Orchard No. 2 Maximum Pressure Buildup of All Layers

Figure 2-64 – Orchard No. 3 Maximum Pressure Buildup of All Layers

Figure 2-65 – Orchard No. 4 Maximum Pressure Buildup of All Layers

Figure 2-66 – Orchard No. 5 Maximum Pressure Buildup of All Layers

Figure 2-67 – Orchard No. 6 Maximum Pressure Buildup of All Layers

Figure 2-68 – Orchard No. 7 Maximum Pressure Buildup of All Layers

After injection ceases, the pressures in the more permeable layers will bleed off rapidly. During the first 10 years post-injection, the maximum pressure falls below the critical Δp value of [redacted] psi, as Figures 2-62 through 2-68 show. Within this time, the maximum Δp value becomes dominated by the lowest permeability grid blocks at or near the wellbore. Those low permeability grid blocks were pressured up due to vertical flow [redacted]. The rate at which the (maximum Δp) pressure declines is dominated by the low permeability in those blocks.

Orchard #1: Pressure Differential from Pre-Injection Values
E-W Cross Section

Figure 2-69 – Orchard No. 1 East-West Cross-Sectional Snapshots of Δp Relative to Pre-injection Pressures (psi)

Orchard #2: Pressure Differential from Pre-Injection Values
E-W Cross Section

Figure 2-70 – Orchard No. 2 East-West Cross-Sectional Snapshots of Δp Relative to Pre-injection Pressures (psi)

Orchard #3: Pressure Differential from Pre-Injection Values
E-W Cross Section

Figure 2-71 – Orchard No. 3 East-West Cross-Sectional Snapshots of Δp Relative to Pre-injection Pressures (psi)

Orchard #4: Pressure Differential from Pre-Injection Values
E-W Cross Section

Figure 2-72 – Orchard No. 4 East-West Cross-Sectional Snapshots of Δp Relative to Pre-injection Pressures (psi)

Figure 2-73 – Orchard No. 5 East-West Cross-Sectional Snapshots of Δp Relative to Pre-injection Pressures (psi)

Figure 2-74 – Orchard No. 6 East-West Cross-Sectional Snapshots of Δp Relative to Pre-injection Pressures (psi)

Orchard #7: Pressure Differential from Pre-Injection Values
E-W Cross Section

Figure 2-75 – Orchard No. 7 East-West Cross-Sectional Snapshots of Δp Relative to Pre-injection Pressures (psi)

2.5 Area of Review Delineation

Title 16 of the Texas Administrative Code (TAC) **§5.203(d)(1)** [Title 40, U.S. Code of Federal Regulations (40 CFR) **§146.84(b)**] requires that an AOR be delineated for a Class VI carbon sequestration well application. The EPA defines the AOR as the greater of either the maximum extent of the separate-phase plume (pore occupancy plume), or the pressure front where the pressure buildup is of sufficient magnitude to force fluids from the injection zone into the formation matrix of a USDW. Both parts of this definition were analyzed to define the Orchard Project AOR.

Figure 2-76 shows a reference line (in red) for the critical pressure differential with a value of [redacted] psi. The extent of the pressure front defined by the value of the critical-pressure differential is used with the pore occupancy plume to define the AOR for the Orchard injection wells.

Figure 2-76 – Stabilized CO_2 Plumes and Critical Pressure Front at the Orchard Project

Figures 2-77 through 2-83 show the injection rates and bottomhole pressures over time for the Orchard injection wells, respectively. The horizontal axis in each is scaled in years, referencing the CO_2 injection startup. Bottomhole pressure (BHP) builds over the [redacted] influenced by overall project-area pressure buildup within the pressure front—pressure that starts to fall off after the injection well is shut in. [redacted] the pressure at each Orchard injector falls below the calculated critical pressure that is required to affect the flow of formation fluids vertically from the injection interval to the deepest known USDW zone.

Figure 2-77 – Injection Rate and BHP Data for Orchard No. 1

Figure 2-78 – Injection Rate and BHP Data for Orchard No. 2

Figure 2-79 – Injection Rate and BHP Data for Orchard No. 3

Figure 2-80 – Injection Rate and BHP Data for Orchard No. 4

Figure 2-81 – Injection Rate and BHP Data for Orchard No. 5

Figure 2-82 – Injection Rate and BHP Data for Orchard No. 6

Figure 2-83 – Injection Rate and BHP Data for Orchard No. 7

Changes in the CO_2 plume over time were illustrated for all seven wells in Figures 2-46 through 2-59 (in *Section 2.4*), with cross-sectional views—east-west and north-south, respectively—of effective CO_2 saturation, comprised of CO_2 in all phases (discussed in *Section 2.2.1*). Those figures presented snapshots of the predicted distribution of the CO_2, taken at the end of injection and 50 years thereafter.

REFERENCES

Barrett, D., & Harpole, K. (1977). Reservoir Data Pays Off: West Seminole San Andres Unit, Gaines County, TX. *52nd Annual Fall Technical Conference and Exhibition of the Society of Petroleum Engineers.* Denver: Society of Petroleum Engineers .

[redacted]

Bennion, B., & Bachu, S. (2005). Relative Permeability Characteristics for Supercritical CO2 Displacing Water in a Variety of Potential Sequestration Zones in the Western Canada Sedimentary Basin. *Paper Number SPE 95547, Presented at the SPE Annual Technical Conference and Exhibition.* Dallas: Society of Petroleum Engineers.

Bennion, D., & Bachu, S. (2008). Drainage and Imbibition Relative Permeability Relationships for Supercritical CO2/Brine and H2S/Brine Systems in Intergranular Sandstone, Carbonate, Shale, and Anhydrite Rocks. *SPE Reservoir Evaluation and Engineering*, 487-496.

Benson, S., Hingerl, F., Zuo, L., Krevor, S., Niu, B., Calvo, R., & Niemi, A. (2015). *Relative Permeability for Multi-phase Flow in CO2 Storage Reservoirs; Part II: Resolving Fundamental Issues and Filling Data Gaps.* Stanford, CA: Stanford University.

Bradley, R., & Kalaswad, S. (2003). *The Groundwater Resources of the Dockum Aquifer in Texas.* Austin: Texas Water Development Board.

Buckley, S., & Leverett, M. (1942). Mechanism of Fluid Displacement in Sands. *Transactions of the AIME*, 107-116.

Corey, A. (1954). The Interrelation Betwen Gas and Oil Relative Permeabilities. *Producers Monthly*, 38-41.

Craft, B., & Hawkins, M. (1959). Undersaturated Oil Reservoirs. In B. Craft, & M. Hawkins, *Applied Petroleum Reservoir Engineering* (pp. 135-136). Englewood Cliffs, NJ: Prentice-Hall Inc.

Crandall, D., Moore, J., Brown, S., & King, S. (2019). *NETL-CO2BRA Relative Permeability Database.* Retrieved from NETL-CO2BRA Relative Permeability Database.

Dykstra, H., & Parsons, R. (1950). The Prediction of Oil Recovery by Waterflooding. In A. P. Production, *Secondary Recovery of Oil in the United States* (pp. 160-174). Washington DC: American Petroleum Institute.

Edwardson, M., Girner, H., Parkison, H., Williamson, C., & Matthew, C. (1962). Calculation of Formation Temperature Distyrbances Caused by Mud Circulation. *Journal of Petroleum Engineering*, 416-426.

Fetkovich, M. (1971). A Simplified Approach to Water Influx Calculations - Finite Aquifer Systems. *Journal of Petroleum Technology*, 814-828.

[redacted]

Harvey, A. (1996). Semiempirical Correlation for Henry's Constants over Large Temperature Ranges. *AIChE Journal*, 1491-1494.

[redacted]

Land, C. (1968). Calculation of Imbibition Relative Permeability for tow- and Three-Phase Flow from Rock Properties. *Society of Petroleum Engineers Journal*, 149-156.

Land, C. S. (1971). Comparison of Calculated with Experimental Imbibition Relative Permeability. *Society Of Petroleum Engineers Journal*, 419-425.

[redacted]

McCain, W. (1991). *The Properties of Petroleum Fluids, Second Edition.* Tulsa: PenWell Books.

Rettman, P., & Leggat, E. (1966). *Ground Water Resources of Gaines County, Texas.* Austin: United States Geological Survey.

Society, R. G. (1956). *Symposium on Oil and Gas Flelds of Southeastern New Mexico.* Roswell, NM: Roswell Geological Society.

Stalkup, F. I. (1983). Principles of Phase Behavior and Miscibility. In F. I. Stalkup, *Miscible Displacement* (pp. 17-22). New York, Dallas: Society of Petroleum Engineers of AIME.

Welge, H. (1952). A Simplified Method for Computing Oil Recovery by Gas or Water Drive. *Petroleum Transactions, AIME*, 91-98.

[redacted]

Appendix 2-1 Water Property Correlations

Density of formation water at standard conditions:

$$\rho_w = 62.368 + 0.438603 \times S + 1.60074 \times 10^{-3} \times S^2$$

This correlation has been found to be as accurate as a laboratory measurement, throughout the full range of solids contents. (McCain, 1991)

Correction of formation water density to reservoir conditions $f(p, T)$:

$$\rho_{w(p,T)} = \rho_w / B_w$$

Formation volume factor of water, B_w, a function of pressure and temperature:

$$B_w = (1 + \Delta V_{wp})(1 + \Delta V_{wp})$$

These correlations are valid for the full range of potential dissolved solids content at temperatures less than 260°F and pressures less than 5,000 psia. (McCain, 1991)

Change in water volume vs. temperature (ΔV_{wT}):

$$\Delta V_{wT} = -1.0001 \times 10^{-2} + 1.33391 \times 10^{-4} \times T + 5.50654 \times 10^{-7} \times T^2$$

Change in water volume vs. pressure (ΔV_{wp}):

$$\Delta V_{wp} = -1.95301 \times 10^{-9} \times (pT) - 1.72834 \times 10^{-13} \times (p^2T) - 3.58922 \times 10^{-7} \times p - 2.25341 \times 10^{-10} \times p^2$$

Nomenclature:

- B_w = *Water formation volume factor vol/vol*
- ρ = *density, lb/ft^3*
- S = *weight percent dissolved solids (equivalent to milligrams per liter* $\times 10^{-4}$)
- T = *Temperature, °F*
- p = *Pressure, psia*

Reference:

McCain, W. (1991). Reservoir-Fluid Property Correlations - State of the Art. *SPE Reservoir Engineering*, 266-272.

Appendix 2-2 Hydrocarbon EOS Parameters in Plume Model

Simulator Fluid Properties

Fluid Properties of Hydrocarbon Components (Used in Peng Robinson EOS):

	CO_2	N_2	CH_4	C_2-C_3	C_4-C_5	C_6-C_8	C_9-C_{14}	C_{15}-C_{29}	C_{30+}
LHC	0.000000	0.000000	1.000000	1.000000	1.000000	1.000000	1.000000	1.000000	1.000000
Vc, l/mol	0.094000	0.089500	0.099000	0.182260	0.288090	0.391550	0.590470	0.995230	1.554890
Acentric f	0.225000	0.040000	0.008000	0.134320	0.225830	0.275570	0.426880	0.737240	1.412020
MW, g/mol	44.010000	28.013000	16.043000	39.412000	66.486000	99.306000	153.481000	305.000000	640.000000
Parachor	78.000000	41.000000	77.000000	112.483000	193.625000	287.663000	432.520000	769.095000	1154.680000
VCMU l/mol	0.094000	0.089500	0.099000	0.182260	0.288090	0.391550	0.590470	0.995230	1.554890
OMEG-A	0.457240	0.457240	0.457240	0.457240	0.457240	0.457240	0.457240	0.457240	0.457240
OMEG-B	0.077796	0.077796	0.077796	0.077796	0.077796	0.077796	0.077796	0.077796	0.077796
EOS-Bc	0.000942	0.000849	0.000946	0.001794	0.002917	0.004028	0.006381	0.012001	0.025058
Pc, atm	72.800000	33.500000	45.400000	43.891000	34.702000	30.974000	23.153000	15.310000	8.737000
tc, K	304.200000	126.200000	190.600000	349.311000	449.039000	553.372000	655.339000	815.000000	971.111000
Zc	0.274140	0.289520	0.287370	0.279080	0.271300	0.267080	0.254220	0.227830	0.170480
SHV/Bc	-0.094347	-0.128390	-0.153860	-0.104130	-0.046518	-0.024895	0.056739	0.073590	0.073804

Binary Interaction Coefficients

CO_2	0								
N_2	0	0							
CH_4	0.105	0.025	0						
C_2-C_3	0.1257	0.06877	0.006179	0					
C_4-C_5	0.11538	0.10261	0.018738	0.003484	0				
C_6-C_8	0.0967	0.11	0.030755	0.009672	0.001567	0			
C_9-C_{14}	0.0874	0.11	0.051036	0.022623	0.008527	0.002807	0		
C_{15}-C_{29}	0.08283	0.11	0.083014	0.046293	0.025114	0.014342	0.004526	0	
C_{30+}	0.11295	0.11	0.115036	0.072271	0.045684	0.030933	0.015437	0.00331	0

Reservoir Hydrocarbon Composition

Component	Mole Fraction
CO_2	0.0027881
N_2	0.0063427
CH_4	0.31149
C_2-C_3	0.0471229
C_4-C_5	0.0950562
C_6-C_8	0.175346
C_9-C_{14}	0.190389
C_{15}-C_{29}	0.148904
C_{30+}	0.0225611

Properties of Reservoir Hydrocarbons

Parameter	Value
Bubble Point – psia	1,656
Reservoir Oil Density – lbm/ft^3	47.9
Reservoir Oil Molecular Weight	185.3
Stock Tank GOR* SCF/STB	415
Stock Tank Oil API Gravity*	36
Stock Tank Gas-Specific Gravity*	0.87

*Stock tank properties based on a single stage flash to standard conditions (60°F, 14.7 psia).